Annals of Mathematical Sciences and Applications
Volume 9, Number 1, 91–121, 2024

A 3D DLM/FD method for simulating the motion of an ellipsoid in a bounded shear flow of viscoelastic fluids

Shang-Huan Chiu and Tsorng-Whay Pan*

In memory of Professor Roland Glowinski

We present a novel distributed Lagrange multiplier/fictitious domain (DLM/FD) method for simulating fluid-particle interaction in viscoelastic fluids in Stokes regime. The results concerning an ellipsoid rotating in a three dimensional (3D) bounded shear flow are obtained for Deborah number (De) up to 4. The averaged angular velocities of a prolate ellipsoid rotating only in the shear plane have been validated in Giesekus fluid and its period of rotation becomes larger when increasing the value of De. For a freely rotating prolate ellipsoid placed in the middle between two moving walls in Oldroyd-B fluids, kayaking motion is stable for lower De and then tilted log-rolling becomes stable when De exceeds a critical value. Similar results are also obtained for a rotating oblate ellipsoid.

AMS 2000 subject classifications: Primary 65M60, 76M10; secondary 76T20.
Keywords and phrases: Oldroyd-B fluid, Giesekus fluid, shear flow, neutrally buoyant ellipsoid, distributed Lagrange multiplier/fictitious domain methods.

1. Introduction

Ellipsoid is a common shape of an object in the nature and can be found everywhere in different scales such as sedimentation [1, 2, 3, 4, 5, 6, 7], bubbles in the fluids [8, 9], colloids [10, 11, 12, 13], and swimmers [14]. There are prolific studies about the motion or behaviors of spherical particle in fluids but relatively rare researches about the ellipsoid due to its complexities [15, 16, 17]. The complexities are not only because of the possible behaviors due to the axisymmetric structure of ellipsoid including the ratio of semi-major and semi-minor axes called aspect ratio (AR) and the initial direction

*Corresponding author.

of ellipsoid's semi-major axis called the initial orientation vector, but also because of the interaction between ellipsoids and fluid due to fluid viscosity, elasticity, and inertia.

For a neutrally buoyant axisymmetric particle rotating in a steady viscous unbounded shear flow of a Newtonian fluid at the Stokes regime, Jeffery [18] found the "Jeffery orbits" which is the existence of infinitely many different periodic orbits and the particular orbit is selected based on the initial orientation vector. As studied in [19], the inertia effects lift the degeneracy of Jeffery orbits and determine the stabilities of the log-rolling and tumbling orbits of ellipsoids rotating at very small Reynolds numbers. For prolate ellipsoids, the tumbling of semi-major axis in the shear plane is stable and log-rolling (i.e., its semi-major axis aligns the vorticity direction) is unstable. On the other hand, for not too disk-like oblate ellipsoids, log-rolling is stable (i.e., its semi-minor axis aligns the vorticity direction) and tumbling of semi-minor axis in the shear plane is unstable. For very flat oblate ellipsoids, both log-rolling and tumbling are stable. But the complexity of non-Newtonian fluids strongly alter the particle dynamics observed in a simple shear flow of Newtonian fluids. For ellipsoid suspensions in a parallel-plate shear flow of non-Newtonian fluids, Gunes *et al.* [20] provided some observations through experiments about how ellipsoids transport in viscoelastic fluids. They found that the increasing shear rate not only causes the period of rotation to become larger but also makes the orientation of ellipsoids changing from the vorticity direction (log-rolling mode) to flow direction and those ellipsoids show the kayaking mode during this process. Abtahi *et al.* [21] investigated the behavior of a prolate spheroid in shear flow of a shear-thinning Carreau fluid and found that shear-thinning rheology does not lift the degeneracy of Jeffery orbits observed in Newtonian fluids, but the instantaneous rate of rotation and trajectories of the orbits are modified.

D'Avino *et al.* [22] studied the motion of prolate ellipsoids in a shear flow of Giesekus viscoelastic fluids without particle inertial effect in Stokes regime. They identified four regions characterized by different dynamical behaviors of an prolate ellipsoid with $AR = 4$ through the Deborah number, which is defined as $De = \dot{\gamma}\lambda_1$ where $\dot{\gamma}$ is the shear rate and λ_1 is the fluid relaxation time. For $De \leq 2$ (region I), the log-rolling motion is stable. For $2 < De < 2.6$ (region II), the semi-major axis is tilted in the flow-vorticity plane with the semi-axis closer to the shear plane for a higher De in this region. In region III, i.e., $2.6 \leq De \leq 2.75$, both tilted and flow alignment orientations coexist. But it needs a very long transient to reach the flow direction. Finally, only alignment along the flow direction is stable for $De > 2.75$ (region IV). Wang *et al.* [23] focused on the motion of neutrally buoyant prolate ellipsoids ($AR = 4$) in a bounded shear flow of Giesekus fluids for De from 0 to 4. Their results are different from those reported in [22] since the effect of fluid and particle inertia is included when studying the rotating motion of prolate ellipsoids. For a prolate ellipsoid with it mass center placed in the middle between two moving walls, before the Deborah number reaches the critical value (between 1.8 and 2), its major axis rotates as a kayaking motion instead of log-rolling. For $De \geq 2$, the prolate ellipsoid moves tilted forwardly and its orientation is closer to the flow direction. But for a prolate ellipsoid placed away from the middle between two walls initially, it migrates toward the nearby wall due to fluid elasticity, and its semi-major axis is turned to the vorticity axis direction (resp., slightly away from the vorticity) during the migration for lower (resp., higher) De values. Li *et al.* [24] investigated the motion of a neutrally buoyant prolate ellipsoid in viscoelastic shear flows with fluid inertia ($\mathrm{Re}_p \neq 0$). For a prolate ellipsoid with larger aspect ratio ($AR = 4$) in a Giesekus fluid with weak fluid inertia, the fluid elasticity increases the particle rotation period and stabilizes its orientation.

To simulate the motion of ellipsoids in a bounded shear flow of Giesekus fluids in three dimensions (3D), we have generalized a distributed Lagrange multiplier/fictitious domain (DLM/FD) method developed in [25] and [26] for simulating the motion of neutrally buoyant particles in either Newtonian or Oldroyd-B fluids in 3D to Giesekus fluids and then combined such method with an operator splitting scheme and a matrix-factorization approach for treating numerically the constitutive equations of the conformation tensor of Giesekus fluids. In this matrix-factorization approach (see [26] and [27]), which is a technique closely related to the one developed by Lozinski and Owens in [28], we solve the equivalent equations so that the semi-positive definiteness of the conformation tensor at the discrete time level can be preserved. In this article, the particle inertia has been considered in simulations since the particle inertia has its effect on the motion of a long body as studied in [19]). This aforementioned method has been validated by comparing the numerical results of a prolate ellipsoid rotating velocity in a bounded shear flow of Giesekus fluids with the results reported in [22]. We have further tested the rotation behaviors of a prolate ellipsoid for the Deborah number up to 4; our results show the prolate rotation dynamics in a bounded shear flow of Oldroyd-B fluids are qualitatively same as those reported in [23] and [24]. For an oblate ellipsoid, it is not surprising to find that its rotating dynamics is closely related to the prolate rotation behaviors. The content of this article is as follows. In Section 2 we present the DLM/FD formulation for an one ellipsoid problem in 3D Giesekus fluid and the related numerical

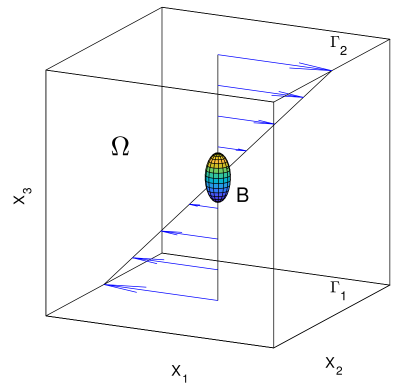

Figure 1: An example of a shear flow region with an ellipsoid.

schemes. In Section 3 we first validate our methodology by comparing numerical results for angular velocity of a prolate ellipsoid with those available in literature. The study of rotation dynamics of prolate and oblate ellipsoids are also presented. Conclusions are summarized in Section 4.

2. Models and numerical methods

2.1. DLM/FD formulation

Fictitious domain formulations using distributed Lagrange multiplier for flow around freely moving particles at finite Reynolds numbers and their associated computational methods have been developed and tested in, e.g., [29, 30, 31, 32, 33, 34, 35]. For simulating the motion of a neutrally buoyant particle in three-dimensional fluid flows of Newtonian and Oldroyd-B fluids at the infinitesimal Reynolds numbers, a similar DLM/FD method has been developed and validated in [25] and [26]. In this section, we discuss first the formulation for the case of an ellipsoid and then the associated numerical treatments for simulating its motion in a 3D bounded shear flow of Giesekus fluids. Let $\Omega \subset \mathbb{R}^3$ be a rectangular parallelepiped filled with a Giesekus fluid and containing a freely moving rigid ellipsoidal particle B centered at $\mathbf{G} = \{G_1, G_2, G_3\}^t$ (see Figure 1). The governing equations are presented in the following

$$-\boldsymbol{\nabla}\cdot\boldsymbol{\sigma}^s - \boldsymbol{\nabla}\cdot\boldsymbol{\tau} = \rho_f \mathbf{g} \quad \text{in} \quad \Omega \setminus \overline{B(t)}, \;\; t \in (0,T), \tag{1}$$

$$\boldsymbol{\nabla}\cdot\mathbf{u} = 0 \quad \text{in} \quad \Omega \setminus \overline{B(t)}, \;\; t \in (0,T), \tag{2}$$

$$\mathbf{u} = \mathbf{g}_0 \ \text{ on } \ \Gamma \times (0,T), \ \text{with} \ \int_\Gamma \mathbf{g}_0 \cdot \mathbf{n}\, d\Gamma = 0, \tag{3}$$

$$\frac{\partial \mathbf{C}}{\partial t} + (\mathbf{u}\cdot\boldsymbol{\nabla})\mathbf{C} - (\boldsymbol{\nabla}\mathbf{u})\mathbf{C} - \mathbf{C}(\boldsymbol{\nabla}\mathbf{u})^t = -\frac{1}{\lambda_1}(\mathbf{C}-\mathbf{I}) - \frac{\alpha}{\lambda_1}(\mathbf{C}-\mathbf{I})^2 \ \text{in} \ \Omega \setminus \overline{B(t)}, \tag{4}$$

$$\mathbf{C}(\mathbf{x},0) = \mathbf{C}_0(\mathbf{x}), \ \mathbf{x} \in \Omega \setminus \overline{B(0)}, \quad \mathbf{C} = \mathbf{C}_L \ \text{on} \ \Gamma^-. \tag{5}$$

In (1), $\mathbf{g}$ denotes gravity and the Cauchy stress tensor $\boldsymbol{\sigma}$ is split into two parts, a Newtonian (solvent) part $\boldsymbol{\sigma}^s$ and a viscoelastic part $\boldsymbol{\tau}$, with:

$$\boldsymbol{\sigma}^s = -p\mathbf{I} + 2\mu\mathbf{D}(\mathbf{u}),$$
$$\boldsymbol{\tau} = \frac{\eta}{\lambda_1}(\mathbf{C}-\mathbf{I}),$$

where $\mathbf{D}(\mathbf{u}) = (\boldsymbol{\nabla}\mathbf{u} + (\boldsymbol{\nabla}\mathbf{u})^t)/2$ is the rate of deformation tensor, $\mathbf{u}$ is the flow velocity, p is the pressure, $\mathbf{C}$ is the conformation tensor, $\mathbf{I}$ is the identity tensor, $\mu = \eta_1\lambda_2/\lambda_1$ is the solvent viscosity of the fluid, $\eta = \eta_1 - \mu$ is the elastic viscosity of the fluid, η_1 is the fluid viscosity, ρ_f is the fluid density, λ_1 is the relaxation time of the fluid, and λ_2 is the retardation time of the fluid. The conformation tensor $\mathbf{C}$ is symmetric and positive definite (see, e.g., [36]). In (3), Γ is the union of the bottom boundary Γ_1 and top boundary Γ_2 as in Figure 1 and $\mathbf{n}$ is the unit normal vector pointing outward to the flow region, $\Gamma^-(t)$ in (5) being the upstream portion of Γ at time t. In (4), α is a constitutive parameter ruling the shear-thinning intensity. (As $\alpha = 0$, (4) is the constitutive equation of Oldroyd-B model without shear thinning). Based on a thermodynamic analysis, the value of α must lay in the range of 0 to 1/2 (see [37] and [38]). The boundary conditions given in (3) are $\mathbf{g}_0 = \{-U, 0, 0\}^t$ on Γ_1 and $\mathbf{g}_0 = \{U, 0, 0\}^t$ on Γ_2 for a bounded shear flow. Hence we have $\Gamma^-(t) = \emptyset$. We assume also that the flow is periodic in the x_1 and x_2 directions with the periods L_1 and L_2, respectively, a no-slip condition taking place on the boundary of particle $\gamma(= \partial B)$, namely

$$\mathbf{u}(\mathbf{x},t) = \mathbf{V}(t) + \boldsymbol{\omega}(t) \times \overrightarrow{\mathbf{G}(t)\mathbf{x}}, \ \forall \mathbf{x} \in \partial B(t), \, t \in (0,T) \tag{6}$$

with $\overrightarrow{\mathbf{G}(t)\mathbf{x}} = \{x_1 - G_1(t), x_2 - G_2(t), x_3 - G_3(t)\}^t$. In addition to (6), the motion of particle B satisfies the following Euler-Newton's equations

$$\frac{d\mathbf{G}}{dt} = \mathbf{V}, \tag{7}$$

$$\frac{d\boldsymbol{\theta}}{dt} = \boldsymbol{\omega}, \tag{8}$$

$$M_p \frac{d\mathbf{V}}{dt} = M_p\,\mathbf{g} + \mathbf{F}_H, \tag{9}$$

$$\frac{d(\mathbf{I}_p\boldsymbol{\omega})}{dt} = \mathbf{T}_H, \tag{10}$$

$$\mathbf{V}(0) = \mathbf{V}_0,\ \boldsymbol{\omega}(0) = \boldsymbol{\omega}_0, \mathbf{G}(0) = \mathbf{G}_0,\ \boldsymbol{\theta}(0) = \boldsymbol{\theta}_0, \tag{11}$$

where M_p and $\mathbf{I}_p$ are the mass and inertia tensor of B, respectively, $\mathbf{V}$ is the velocity of the center of mass, $\boldsymbol{\omega}$ is the angular velocity and $\boldsymbol{\theta}$ is the inclination angle of the particle. The hydrodynamic forces and torque are given by

$$\mathbf{F}_H = -\int_{\partial B} \boldsymbol{\sigma}\mathbf{n}\, ds, \quad \mathbf{T}_H = -\int_{\partial B} \overrightarrow{\mathbf{Gx}} \times \boldsymbol{\sigma}\mathbf{n}\, ds. \tag{12}$$

Remark 1. As reported in [19], at the infinitesimal Reynolds numbers, the particle and fluid inertial effects determine the stability of a prolate ellipsoid rotating motion in a shear flow of a Newtonian fluid. Its major axis tumbling in the shear plane is stable and the motion of a prolate ellipsoid rotating with respect to its major axis perpendicular to the shear plane (so called log-rolling) is unstable. With only the effect of particle inertia, similar results of a prolate ellipsoid rotating in a shear flow of a Newtonian fluid were also obtained in [25] via a DLM/FD formulation at the Stokes regime. In this article, via the above problem (1)–(12), we would like to study the effect of particle inertia on the motion of ellipsoids in viscoelastic fluids at the infinitesimal Reynolds numbers (i.e., without the fluid inertia effect). □

To obtain a distributed Lagrange multiplier/fictitious domain formulation for the above problem (1)–(12), we proceed as in [29, 31], namely: (i) we derive first a global variational formulation (of the virtual power type) of problem (1)–(12), (ii) we then fill the region occupied by the rigid body by the surrounding fluid (i.e., embed $\Omega \setminus \overline{B(t)}$ in Ω) with a constraint that the fluid inside the rigid body region has a rigid body motion, and then (iii) we relax the rigid body motion constraint by using a distributed Lagrange multiplier, obtaining thus the following fictitious domain formulation over the entire region Ω:

For a.e. $t \in (0,T)$, find $\mathbf{u}(t) \in \mathbf{V}_{\mathbf{g}_0}$, $p(t) \in L^2_0(\Omega)$, $\mathbf{C}(t) \in V_{\mathbf{C}}$, $\mathbf{V}(t) \in \mathbb{R}^3$,

$\mathbf{G}(t) \in \mathbb{R}^3$, $\boldsymbol{\omega}(t) \in \mathbb{R}^3$, $\boldsymbol{\lambda}(t) \in \Lambda(t)$ such that

$$(13) \quad \begin{cases} -\int_\Omega p\boldsymbol{\nabla}\cdot\mathbf{v}d\mathbf{x} + 2\mu\int_\Omega \mathbf{D}(\mathbf{u}):\mathbf{D}(\mathbf{v})\,d\mathbf{x} - \int_\Omega (\boldsymbol{\nabla}\cdot\boldsymbol{\tau})\cdot\mathbf{v}\,d\mathbf{x} \\ \quad - < \boldsymbol{\lambda}, \mathbf{v} - \mathbf{Y} - \boldsymbol{\xi}\times\overrightarrow{\mathbf{Gx}} >_{\Lambda(t)} + M_p\dfrac{d\mathbf{V}}{dt}\cdot\mathbf{Y} \\ \quad + \dfrac{d(\mathbf{I}_p\boldsymbol{\omega})}{dt}\cdot\boldsymbol{\xi} = \left(1 - \dfrac{\rho_f}{\rho_s}\right)M_p\,\mathbf{g}\cdot\mathbf{Y} + \rho_f\int_\Omega \mathbf{g}\cdot\mathbf{v}\,d\mathbf{x}, \\ \quad \forall\mathbf{v}\in\mathbf{V}_0, \quad \forall\mathbf{Y}\in\mathbb{R}^3, \quad \forall\boldsymbol{\xi}\in\mathbb{R}^3, \end{cases}$$

$$(14) \quad \int_\Omega q\boldsymbol{\nabla}\cdot\mathbf{u}(t)\,d\mathbf{x} = 0, \ \forall q \in L^2(\Omega),$$

$$(15) \quad < \boldsymbol{\mu}, \mathbf{u}(t) - \mathbf{V}(t) - \boldsymbol{\omega}(t)\times\overrightarrow{\mathbf{Gx}} >_{\Lambda(t)} = 0, \ \forall\boldsymbol{\mu}\in\Lambda(t),$$

$$(16) \quad \int_\Omega \left(\frac{\partial\mathbf{C}}{\partial t} + (\mathbf{u}\cdot\boldsymbol{\nabla})\mathbf{C} - (\boldsymbol{\nabla}\mathbf{u})\mathbf{C} - \mathbf{C}(\boldsymbol{\nabla}\mathbf{u})^t\right) : \mathbf{s}\,d\mathbf{x}$$

$$(17) \quad = -\int_\Omega \frac{1}{\lambda_1}(\mathbf{C}-\mathbf{I}) : \mathbf{s}\,d\mathbf{x} - \int_\Omega \frac{\alpha}{\lambda_1}(\mathbf{C}-\mathbf{I})^2 : \mathbf{s}\,d\mathbf{x}, \\ \forall\mathbf{s}\in\mathbf{V}_{\mathbf{C}}, \text{with } \mathbf{C} = \mathbf{I} \text{ in } B(t),$$

$$(18) \quad \frac{d\mathbf{G}}{dt} = \mathbf{V},$$

$$(19) \quad \mathbf{C}(\mathbf{x},0) = \mathbf{C}_0(\mathbf{x}), \forall\mathbf{x}\in\Omega, \text{with } \mathbf{C}_0 = \mathbf{I} \text{ in } B(0),$$

$$(20) \quad \mathbf{G}(0) = \mathbf{G}_0, \ \mathbf{V}(0) = \mathbf{V}_0, \ \boldsymbol{\omega}(0) = \boldsymbol{\omega}_0, \ B(0) = B_0,$$

where the function spaces in problem (13)–(20) are defined by

$$\begin{aligned} \mathbf{V}_{\mathbf{g}_0} &= \{\mathbf{v}|\mathbf{v}\in(H^1(\Omega))^3, \ \mathbf{v} = \mathbf{g}_0 \text{ on } \Gamma, \ \mathbf{v} \text{ is periodic in the } x_1 \text{ and} \\ &\qquad x_2 \text{ directions with periods } L_1 \text{ and } L_2, \text{ respectively}\}, \\ \mathbf{V}_0 &= \{\mathbf{v}|\mathbf{v}\in(H^1(\Omega))^3, \ \mathbf{v} = \mathbf{0} \text{ on } \Gamma, \ \mathbf{v} \text{ is periodic in the } x_1 \text{ and } x_2 \\ &\qquad \text{directions with periods } L_1 \text{ and } L_2, \text{ respectively}\}, \\ L_0^2(\Omega) &= \left\{q|q\in L^2(\Omega), \ \int_\Omega q\,d\mathbf{x} = 0\right\}, \\ \mathbf{V}_{\mathbf{C}} &= \{\ \mathbf{C} \mid \mathbf{C}\ \in (H^1(\Omega))^{3\times3}, \ \mathbf{C} \text{ is periodic in the } x_1 \text{ and } x_2 \\ &\qquad \text{directions with periods } L_1 \text{ and } L_2, \text{ respectively}\}, \\ \Lambda(t) &= (H^1(B(t)))^3, \end{aligned}$$

and for any $\boldsymbol{\mu}\in H^1(B(t))^3$ and any $\mathbf{v}\in\mathbf{V}_0$, the pairing $< \cdot,\cdot >_{\Lambda(t)}$ in (13) and (15) is defined by

$$< \boldsymbol{\mu}, \mathbf{v} >_{\Lambda(t)} = \int_{B(t)} (\boldsymbol{\mu} \cdot \mathbf{v} + d^2 \boldsymbol{\nabla} \boldsymbol{\mu} : \boldsymbol{\nabla} \mathbf{v}) \, d\mathbf{x}$$

where d is a scaling constant, a typical choice for d being the diameter of particle B.

Remark 2. In relation (13), the term $2\int_\Omega \mathbf{D}(\mathbf{u}){:}\mathbf{D}(\mathbf{v}) \, d\mathbf{x}$ can be replaced by $\int_\Omega \boldsymbol{\nabla}\mathbf{u}{:}\boldsymbol{\nabla}\mathbf{v} \, d\mathbf{x}$. Also the gravity term $\mathbf{g}$ in (13) can be absorbed into the pressure term. □

Remark 3. We use two normal vectors to track the orientation of the ellipsoid and $\mathbf{x}_1$, $\mathbf{x}_2$ are the points of the tips of the vectors. The actions of $\mathbf{x}_1$ and $\mathbf{x}_2$ are described by the following equations

$$\frac{d\mathbf{x}_i}{dt} = \mathbf{V}(t) + \boldsymbol{\omega}(t) \times \overrightarrow{\mathbf{G}(t)\mathbf{x}_i}, \mathbf{x}_i(0) = \mathbf{x}_{i,0}, \ i = 1, 2.$$

□

Remark 4. In the system (13)–(20), the treatment of neutrally buoyant particles is quite different from those considered in, e.g., [32, 33, 34] for the cases of neutrally buoyant particles in incompressible viscous flow modeled by the full Navier-Stokes equations. For the particle-flow interaction under creeping flow conditions considered in this article, there is no need to add any extra constraint on the Lagrange multiplier as in [32, 33, 34]. □

2.2. Numerical methods

For the space discretization, we have chosen P_1-*iso*-P_2 and P_1 finite element spaces for the velocity field and pressure, respectively, (like in Bristeau et al. [39] and Glowinski [40]), that is

$$\begin{aligned}
\mathbf{W}_h &= \{\mathbf{v}_h | \mathbf{v}_h \in (C^0(\overline{\Omega}))^3, \mathbf{v}_h|_T \in (P_1)^3, \forall T \in \mathcal{T}_h, \mathbf{v}_h \textit{ is periodic in the} \\
&\qquad x_1 \textit{ and } x_2 \textit{ directions with the periods } L_1 \textit{ and } L_2\textit{, respectively}\}, \\
\mathbf{W}_{0h} &= \{\mathbf{v}_h | \mathbf{v}_h \in \mathbf{W}_h, \ \mathbf{v}_h = \mathbf{0} \text{ on } \Gamma\}, \\
L^2_h &= \{q_h | q_h \in C^0(\overline{\Omega}), \ q_h|_T \in P_1, \ \forall T \in \mathcal{T}_{2h}, \ q_h \textit{ is periodic in the } x_1 \\
&\qquad \textit{and } x_2 \textit{ directions with the periods } L_1 \textit{ and } L_2\textit{, respectively}\}, \\
L^2_{0h} &= \left\{ q_h | q_h \in L^2_h, \ \int_\Omega q_h \, d\mathbf{x} = 0 \right\},
\end{aligned}$$

where h is the space discretization mesh size, $\mathcal{T}_h$ is a regular tetrahedral mesh covering Ω, $\mathcal{T}_{2h}$ is another tetrahedral mesh also covering Ω, twice

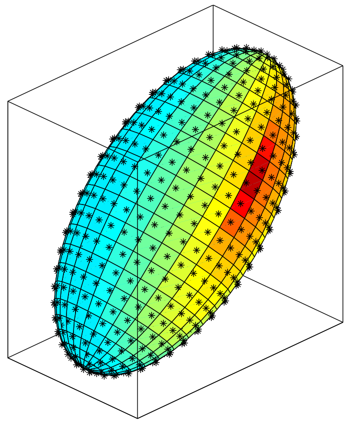

Figure 2: An example of collocation points chosen on ∂B.

coarser than $\mathcal{T}_h$, and P_1 is the space of the polynomials in three variables of degree ≤ 1. The finite dimensional space for approximating $\mathbf{V_C}$ is defined by

$$\mathbf{V}_{\mathbf{C}_h} = \{\mathbf{s}_h | \mathbf{s}_h \in (C^0(\overline{\Omega}))^{3\times 3}, \mathbf{s}_h|_T \in (P_1)^{3\times 3}, \forall T \in \mathcal{T}_h,\ \mathbf{s}_h \textit{ is periodic in the } x_1 \textit{ and } x_2 \textit{ directions with the periods } L_1 \textit{ and } L_2\textit{, respectively}\}.$$

For simulating the particle motion in fluid flows, a typical finite dimensional space approximating $\Lambda(t)$ (e.g., see [31, 33, 34]) is defined as follows: let $\{\mathbf{y}_i\}_{i=1}^{N(t)}$ be a set of points covering $\overline{B(t)}$; the discrete multiplier space $\Lambda_h(t)$ is defined by

$$\Lambda_h(t) = \left\{ \boldsymbol{\mu}_h | \boldsymbol{\mu}_h = \sum_{i=1}^{N(t)} \boldsymbol{\mu}_i \delta(\mathbf{x} - \mathbf{y}_i),\ \boldsymbol{\mu}_i \in \mathbb{R}^3,\ \forall i = 1, \dots, N(t) \right\}, \tag{21}$$

where $\delta(\cdot)$ is the Dirac measure at $\mathbf{x} = \mathbf{0}$. Then, we define a pairing over $\Lambda_h(t) \times \mathbf{W}_{0h}$ by

$$< \boldsymbol{\mu}_h, \mathbf{v}_h >_{\Lambda_h(t)} = \sum_{i=1}^{N(t)} \boldsymbol{\mu}_i \cdot \mathbf{v}_h(\mathbf{y}_i),\ \forall \boldsymbol{\mu}_h \in \Lambda_h(t),\ \mathbf{v}_h \in \mathbf{W}_{0h}. \tag{22}$$

A typical set $\{\mathbf{y}_j\}_{j=1}^{N(t)}$ of the points of $\overline{B}(t)$ to be used in (22) is defined as

$$\{\mathbf{y}_j\}_{j=1}^{N(t)} = \{\mathbf{y}_j\}_{j=1}^{N_1(t)} \cup \{\mathbf{y}_j\}_{j=N_1(t)+1}^{N(t)}$$

where $\{\mathbf{y}_j\}_{j=1}^{N_1(t)}$ (resp., $\{\mathbf{y}_j\}_{j=N_1(t)+1}^{N(t)}$) is the set of those vertices of the velocity grid $\mathcal{T}_h$ contained in $B(t)$ and whose distance to $\partial B(t) \geq h/2$ (resp., is a set of selected points of $\partial B(t)$, as shown in Fig. 2). As in [25] and [26], for simulating particle interactions in Stokes flow, we have modified the discrete pairing $< \cdot, \cdot >_{\Lambda_h(t)}$ as follows:

$$\begin{aligned} < \boldsymbol{\mu}_h, \mathbf{v}_h >_{\Lambda_h(t)} = & \sum_{i=1}^{N_1(t)} \boldsymbol{\mu}_i \cdot \mathbf{v}_h(\mathbf{y}_i) \\ & + \sum_{i=N_1(t)+1}^{N(t)} \sum_{j=1}^{M} \boldsymbol{\mu}_i \cdot \mathbf{v}_h(\mathbf{y}_i)\ D_h(\mathbf{y}_i - \mathbf{x}_j)\ h^3, \end{aligned} \tag{23}$$

for $\boldsymbol{\mu}_h \in \Lambda_h(t)$ and $\mathbf{v}_h \in \mathbf{W}_{0h}$ where h is the uniform finite element mesh size for the velocity field, $\{\mathbf{x}_j\}_{j=1}^{M}$ is the set of grid points of the velocity field, and the function $D_h(\mathbf{X} - \boldsymbol{\xi})$ is defined as

$$D_h(\mathbf{X} - \boldsymbol{\xi}) = \delta_h(X_1 - \boldsymbol{\xi}_1)\delta_h(X_2 - \boldsymbol{\xi}_2)\delta_h(X_3 - \boldsymbol{\xi}_3) \tag{24}$$

with $\mathbf{X} = \{X_1, X_2, X_3\}^t$, $\boldsymbol{\xi} = \{\boldsymbol{\xi}_1, \boldsymbol{\xi}_2, \boldsymbol{\xi}_3\}^t$, the one–dimensional approximate Dirac measure δ_h being defined by

$$\delta_h(s) = \begin{cases} \frac{1}{8h}\Big(3 - \frac{2|s|}{h} + \sqrt{1 + \frac{4|s|}{h} - 4(\frac{|s|}{h})^2}\Big), & |s| \leq h, \\ \frac{1}{8h}\Big(5 - \frac{2|s|}{h} - \sqrt{-7 + \frac{12|s|}{h} - 4(\frac{|s|}{h})^2}\Big), & h \leq\ |s| \leq 2h, \\ 0, & \text{otherwise.} \end{cases} \tag{25}$$

The above approximate delta functions δ_h and D_h are the typical ones used in the popular immersed boundary method developed by Peskin, e.g, [41, 42, 43].

To fully discretize system (13)–(20), we reduce it first to a finite dimensional initial value problem using the above finite element spaces (after dropping most of the sub-scripts h's). Next, we combine the Lozinski-Owens factorization approach (see, e.g., [27, 28]) with the Lie scheme (e.g., see [44, 45]) to decouple the above finite element analogue of system (13)–(20) into a sequence of sub-problems and apply the backward Euler schemes to time-discretize some of these sub-problems. Finally we obtain thus the following sequence of sub-problems (where $\triangle t(> 0)$ is a time-discretization step and $t^n = n\triangle t$):

$$\mathbf{C}^0 = \mathbf{C}_0, \mathbf{G}^0 = \mathbf{G}_0, \mathbf{V}^0 = \mathbf{V}_0, \text{and } \boldsymbol{\omega}^0 = \boldsymbol{\omega}_0 \text{ are given;} \tag{26}$$

For $n \geq 0$, $\mathbf{C}^n$, $\mathbf{G}^n$, $\mathbf{V}^n$, $\boldsymbol{\omega}^n$ being known, we compute the approximate solution at $t = t^{n+1}$ via the following fractional steps:

1. We first predict the position and the translation velocity of the center of mass as follows:

$$\frac{d\mathbf{G}}{dt} = \mathbf{V}(t), \tag{27}$$

$$M_p \frac{d\mathbf{V}}{dt} = \mathbf{0}, \tag{28}$$

$$\frac{d(\mathbf{I}_p\boldsymbol{\omega})}{dt} = \mathbf{0}, \tag{29}$$

$$\frac{d\mathbf{x}_i}{dt} = \mathbf{V}(t) + \boldsymbol{\omega}(t) \times \overrightarrow{\mathbf{G}(t)\mathbf{x}_i},\ x_i(t^n) = \mathbf{x}_i^n, i = 1, 2, \tag{30}$$

$$\mathbf{V}(t^n) = \mathbf{V}^n, (\mathbf{I}_p\boldsymbol{\omega})(t^n) = (\mathbf{I}_p\boldsymbol{\omega})^n, \mathbf{G}(t^n) = \mathbf{G}^n, \tag{31}$$

   for $t^n < t < t^{n+1}$. Then set $\mathbf{V}^{n+\frac{1}{5}} = \mathbf{V}(t^{n+1})$, $(\mathbf{I}_p\boldsymbol{\omega})^{n+\frac{1}{5}} = (\mathbf{I}_p\boldsymbol{\omega})(t^{n+1})$, $\mathbf{G}^{n+\frac{1}{5}} = \mathbf{G}(t^{n+1})$, $\mathbf{x}_1^{n+\frac{1}{5}} = \mathbf{x}_1(t^{n+1})$, and $\mathbf{x}_2^{n+\frac{1}{5}} = \mathbf{x}_2(t^{n+1})$. After the center $\mathbf{G}^{n+\frac{1}{5}}$ and $\mathbf{x}_1^{n+\frac{1}{5}}$, $\mathbf{x}_2^{n+\frac{1}{5}}$ are known, the position $B^{n+\frac{1}{5}}$ occupied by the particle is determined.
2. Next, we enforce the rigid body motion in $B^{n+\frac{1}{5}}$ and solve for $\mathbf{u}^{n+\frac{2}{5}}$, $p^{n+\frac{2}{5}}$, $\mathbf{V}^{n+\frac{2}{5}}$ and $\boldsymbol{\omega}^{n+\frac{2}{5}}$ simultaneously as follows:
   Find $\mathbf{u}^{n+\frac{2}{5}} \in \mathbf{W}_h$, $\mathbf{u}^{n+\frac{2}{5}} = \mathbf{g}_{0h}$ on Γ, $p^{n+\frac{2}{5}} \in L^2_{0h}$, $\boldsymbol{\lambda}^{n+\frac{2}{5}} \in \Lambda_h^{n+\frac{1}{5}}$, $\mathbf{V}^{n+\frac{2}{5}} \in \mathbb{R}^3$, $\boldsymbol{\omega}^{n+\frac{2}{5}} \in \mathbb{R}^3$ so that

$$\begin{cases} -\int_\Omega p^{n+\frac{2}{5}} \boldsymbol{\nabla} \cdot \mathbf{v}\, d\mathbf{x} + \mu \int_\Omega \boldsymbol{\nabla}\mathbf{u}^{n+\frac{2}{5}} : \boldsymbol{\nabla}\mathbf{v}\, d\mathbf{x} \\ \quad - \int_\Omega \left(\boldsymbol{\nabla} \cdot \frac{\eta}{\lambda_1}(\mathbf{C}^n - \mathbf{I}) \right) \cdot \mathbf{v}\, d\mathbf{x} + M_p \frac{\mathbf{V}^{n+\frac{2}{5}} - \mathbf{V}^{n+\frac{1}{5}}}{\triangle t} \cdot \mathbf{Y} \\ \quad + \frac{\mathbf{I}_p^{n+\frac{1}{5}} \boldsymbol{\omega}^{n+\frac{2}{5}} - (\mathbf{I}_p\boldsymbol{\omega})^{n+\frac{1}{5}}}{\triangle t} \cdot \boldsymbol{\xi} = \left(1 - \frac{\rho_f}{\rho_s}\right) M_p \mathbf{g} \cdot \mathbf{Y} \\ \quad + < \boldsymbol{\lambda}^{n+\frac{2}{5}},\ \mathbf{v} - \mathbf{Y} - \boldsymbol{\xi} \times \overrightarrow{\mathbf{G}^{n+\frac{1}{5}}\mathbf{x}} >_{\Lambda_h^{n+\frac{1}{5}}}, \\ \quad \forall \mathbf{v} \in \mathbf{W}_{0h},\ \mathbf{Y} \in \mathbb{R}^3,\ \boldsymbol{\xi} \in \mathbb{R}^3, \end{cases} \tag{32}$$

$$\int_\Omega q \boldsymbol{\nabla} \cdot \mathbf{u}^{n+\frac{2}{5}}\, d\mathbf{x} = 0,\ \forall q \in L^2_h, \tag{33}$$

$$< \boldsymbol{\mu}, \mathbf{u}^{n+\frac{2}{5}} - \mathbf{V}^{n+\frac{2}{5}} - \boldsymbol{\omega}^{n+\frac{2}{5}} \times \overrightarrow{\mathbf{G}^{n+\frac{1}{5}}\mathbf{x}} >_{\Lambda_h^{n+\frac{1}{5}}} = 0,\ \forall \boldsymbol{\mu} \in \Lambda_h^{n+\frac{1}{5}}. \tag{34}$$

3. We then compute $\mathbf{A}^{n+\frac{3}{5}}$ via the solution of

$$(35)\quad \begin{cases} \displaystyle\int_\Omega \frac{\partial \mathbf{A}(t)}{\partial t} : \mathbf{s}\, d\mathbf{x} + \int_\Omega (\mathbf{u}^{n+\frac{2}{5}} \cdot \boldsymbol{\nabla})\mathbf{A}(t) : \mathbf{s}\, d\mathbf{x} = 0, \forall \mathbf{s} \in \mathbf{V}_{\mathbf{A}_h}, \\ \mathbf{A}(t^n) = \mathbf{A}^n, \text{ where } \mathbf{A}^n(\mathbf{A}^n)^t = \mathbf{C}^n, \\ \mathbf{A}(t) \in \mathbf{V}_{\mathbf{A}_h}, \, t \in [t^n, t^{n+1}], \end{cases}$$

and set $\mathbf{A}^{n+\frac{3}{5}} = \mathbf{A}(t^{n+1})$.

4. We then compute $\mathbf{A}^{n+\frac{4}{5}}$ via the solution of

$$(36)\quad \begin{cases} \displaystyle\int_\Omega \left(\frac{\mathbf{A}^{n+\frac{4}{5}} - \mathbf{A}^{n+\frac{3}{5}}}{\triangle t} - (\boldsymbol{\nabla}\mathbf{u}^{n+\frac{2}{5}})\mathbf{A}^{n+\frac{4}{5}} + \frac{1}{2\lambda_1}\mathbf{A}^{n+\frac{4}{5}} \right) : \mathbf{s}\, d\mathbf{x} = 0, \\ \forall \mathbf{s} \in \mathbf{V}_{\mathbf{A}_h}; \mathbf{A}^{n+\frac{4}{5}} \in \mathbf{V}_{\mathbf{A}_h}. \end{cases}$$

and set

$$(37)\quad \mathbf{C}^{n+\frac{4}{5}} = \mathbf{A}^{n+\frac{4}{5}}(\mathbf{A}^{n+\frac{4}{5}})^t + \frac{\triangle t}{\lambda_1}\mathbf{I}.$$

5. Finally we obtain $\mathbf{C}^{n+1}$ via the solution of

$$(38)\quad \begin{cases} \displaystyle\int_\Omega \left(\frac{\mathbf{C}^{n+1} - \mathbf{C}^{n+\frac{4}{5}}}{\triangle t} + \frac{\alpha}{\lambda_1}(\mathbf{C}^{n+\frac{4}{5}} - \mathbf{I})^2 \right) : \mathbf{s}\, d\mathbf{x} = 0, \\ \forall \mathbf{s} \in \mathbf{V}_{\mathbf{C}_h}; \mathbf{C} \in \mathbf{V}_{\mathbf{C}_h}, \end{cases}$$

and set

$$(39)\quad \mathbf{C}^{n+1} = \mathbf{I} \text{ in } B^{n+\frac{1}{5}}.$$

Set $\mathbf{G}^{n+1} = \mathbf{G}^{n+\frac{1}{5}}$, $\mathbf{x}_1^{n+1} = \mathbf{x}_1^{n+\frac{1}{5}}$, $\mathbf{x}_2^{n+1} = \mathbf{x}_2^{n+\frac{1}{5}}$, $\mathbf{V}^{n+1} = \mathbf{V}^{n+\frac{2}{5}}$, and $(\mathbf{I}_p\boldsymbol{\omega})^{n+1} = \mathbf{I}_p^{n+\frac{1}{5}}\boldsymbol{\omega}^{n+\frac{2}{5}}$.

In (35)–(37), the space $\mathbf{V}_{\mathbf{A}_h}$ is defined similarly to $\mathbf{V}_{\mathbf{C}_h}$. The multiplier space $\Lambda_h^{n+\frac{1}{5}}$ in (32)–(34) is defined according to the position of $B^{n+\frac{1}{5}}$.

2.3. On the solution of the sub-problems

In system (32)–(34), there are two multipliers, namely, p and $\boldsymbol{\lambda}$. We have solved this system via an Uzawa-conjugate gradient method driven by both multipliers developed in [25, 46] for 2D and 3D flow simulations. Problems (26)–(31) is just a system of ordinary differential equations. They are solved using the forward Euler method with a sub-time step to predict the translation velocity of the mass center and then the position of mass center. At the steps 3 and 4 of algorithm (27)–(39), we have considered the equations verified by $\mathbf{A}$ instead of those verified by the conformation tensor $\mathbf{C}$ due to the use of a factorization approach (e.g., see [27] for details). In the implementation, this kind of the Lozinski-Owens' scheme relies on the matrix factorization $\mathbf{C} = \mathbf{A}\mathbf{A}^T$ of the conformation tensor, and then on a reformulation in terms of $\mathbf{A}$ of the time dependent equation modeling the evolution of $\mathbf{C}$, providing automatically that $\mathbf{C}$ is at least positive semi-definite (and symmetric). The matrix factorization based method introduced in [28] has been applied, via an operator splitting scheme coupled to a FD/DLM method, to the simulation of two-dimensional and three-dimensional particulate flows of Oldroyd-B in, e.g., [26, 27, 35, 47]. The equation (35) is a pure advection problem. We solve this equation by a wave-like equation method (see, e.g., [45, 48]) which is a numerical dissipation free explicit method. Since the advection problem is decoupled from the other ones, we can choose a proper sub-time step so that the CFL condition is satisfied.

Problem (36) gives a simple equation at each grid point which can be solved easily if we use trapezoidal quadrature rule to compute the integrals. The value of $\boldsymbol{\nabla}\mathbf{u}^{n+\frac{2}{5}}$ at each interior grid node is obtained by the averaged value of those values computed in all tetrahedral elements having the grid node as a vertex, however for the grid node on Γ it is obtained by applying linear extrapolation via the values of two neighboring interior nodes as discussed in [49]. Problem (38) can be solved by a similar approach. Instead of having time discretization by the backward Euler's method to obtain problem (36), let's consider its differential equation at each grid point as follows

$$\frac{\partial \mathbf{A}}{\partial t} - (\boldsymbol{\nabla}\mathbf{U})\mathbf{A} + \frac{1}{2\lambda_1}\mathbf{A} = \mathbf{0}, \; t^n < t < t^{n+1}, \; \mathbf{A}(t^n) = \mathbf{A}_0, \tag{40}$$

where the initial condition is $\mathbf{A}_0 = \mathbf{A}^{n+3/5}$ and the approximation of $\boldsymbol{\nabla}\mathbf{U}$ is computed by the 2nd order schemes developed in [49] for $\mathbf{U} = \mathbf{u}^{n+\frac{2}{5}}$. The closed-form solution of (40) is

$$\mathbf{A}(t) = e^{-\frac{(t-t^n)}{2\lambda_1}} e^{(t-t^n)\boldsymbol{\nabla}\mathbf{U}} \; \mathbf{A}_0, \tag{41}$$

which can be easily incorporated into algorithm (26)–(39). The above closed-form solution has been adapted to obtain numerical solutions reported in [35]. When solving Giesekus fluid flow problem, the differential equation at each grid point of problem (38) is

$$\frac{d\mathbf{C}}{dt} = -\frac{\alpha}{\lambda_1}(\mathbf{C}-\mathbf{I})^2,\ t^n < t < t^{n+1},\ \mathbf{C}(t^n) = \mathbf{C}_0, \tag{42}$$

where the initial condition is $\mathbf{C}_0 = \mathbf{C}^{n+\frac{4}{5}}$. The closed-form solution of problem (42) is

$$\mathbf{C}(t) = \left(\mathbf{C}_0 + \frac{\alpha}{\lambda_1}(\mathbf{C}_0-\mathbf{I})(t-t^n)\right)\left(\mathbf{I} + \frac{\alpha}{\lambda_1}(\mathbf{C}_0-\mathbf{I})(t-t^n)\right)^{-1}. \tag{43}$$

This closed-form solution can also be combined easily with algorithm (26)–(39).

In [26], we have combined our DLM/FD method with an operator splitting scheme and matrix-factorization approach to numerically treat the constitutive equations of the conformation tensor of Oldroyd-B fluids. In this article, we have generalized the technique developed in [26] to solve the Stokes equation coupling with an ellipsoid rotating in a Giesekus fluid. For $\alpha = 0$ in (4) and (16), step 5 in algorithm (26)–(39) has been dropped for an Oldroyd-B fluid, but the closed-form solution in (41) has been used instead of solving problem (36). For $\alpha \neq 0$, the solution of problem (38) is directly computed from the closed-form solution (43).

3. Numerical results and discussion

3.1. A prolate ellipsoid rotating in the shear plane

We have considered the cases of a neutrally buoyant ellipsoid which is placed at the middle between two moving walls initially as shown in Fig. 3 in a bounded shear flow of Giesekus fluids as constitutive parameter $\alpha = 0.2$. The densities of the fluid and that of the particle are $\rho_f = \rho_s = 1\ \mathrm{g\,cm^{-3}}$ and the viscosity $\mu_f = 1$ poise. The computational domain is $\Omega = (-H/2, H/2) \times (-H/2, H/2) \times (-H/2, H/2)$ for $H = 4$ cm. The shear rate $\dot\gamma = 1\ sec^{-1}$ so the speed of the top wall is $U = H/2$ cm/sec and that of the bottom wall is $-U = -H/2$ cm/sec. The mesh sizes for velocity field are $h = 1/24$, $1/32$, and $1/48$, the mesh size for the pressure is $2h$, and the time step is $\triangle t = 0.001$. The Deborah number is $De = \dot\gamma\lambda_1$. For all the numerical

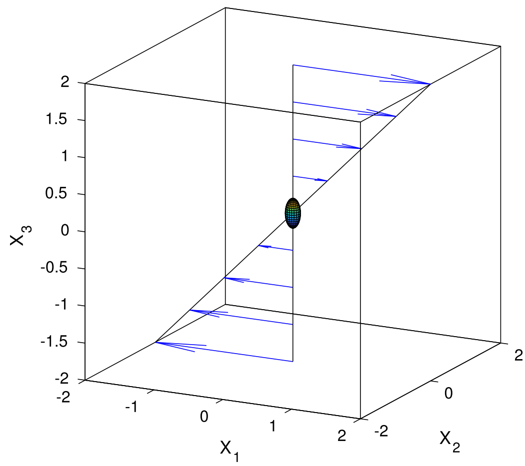

Figure 3: A single prolate ellipsoid in a two wall driven bounded shear flow with its mass center at (0, 0, 0).

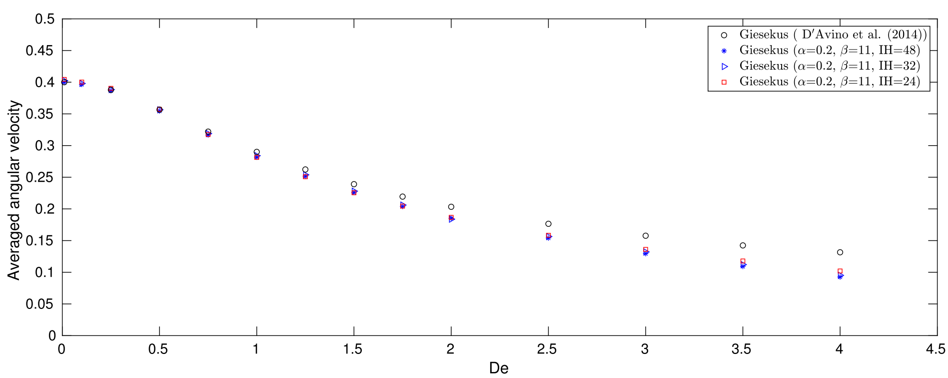

Figure 4: Comparison of the averaged angular velocity of a single prolate ellipsoid rotating in Giesekus fluids for different values of De $(= \lambda_1 \dot{\gamma})$.

simulations, we assume that all dimensional quantities are in the centimeter, gram and second units.

To study the rotating angular velocity of a prolate ellipsoid, we consider the mass center of ellipsoid is fixed at $(0, 0, 0)$ with $\lambda_1 = 0.01$, 0.1, 0.25, 0.5, 0.75, 1.0, 1.25, 1.5, 1.75, 2.0, 2.5, 3.0, 3.5, 4.0 sec. The retardation time is $\lambda_2 = \beta\lambda_1 = \lambda_1/11$. The semi-major and two semi-minor axes are $a = 0.2$ cm and $b = c = 0.1$ cm, the major axis and one of the minor axis being on the x_1x_3-plane with an initial inclination angle of 0 with

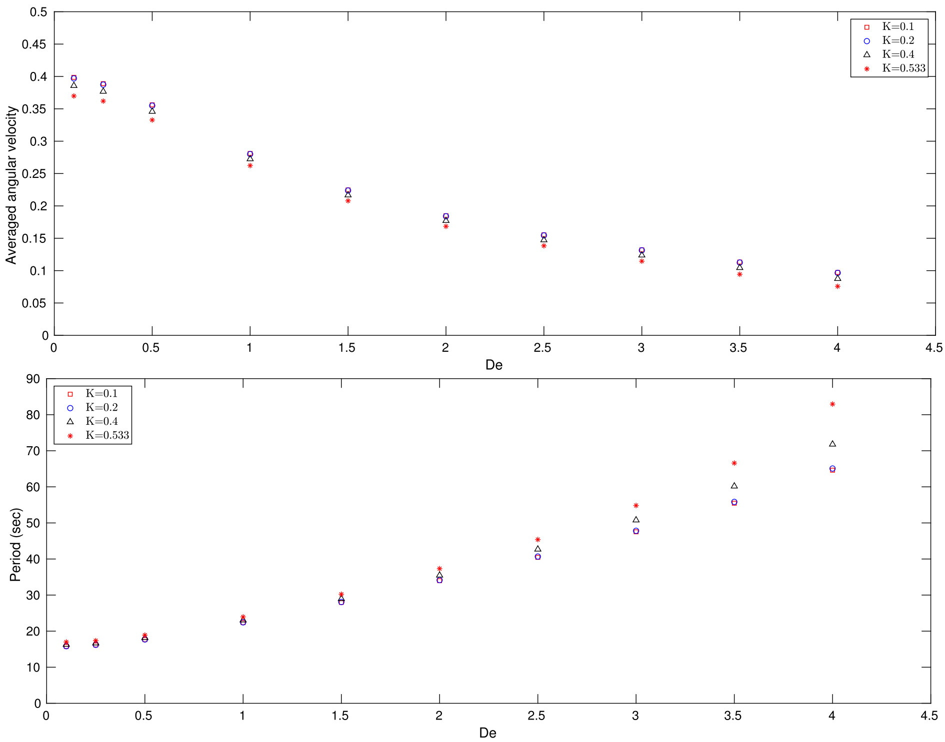

Figure 5: The averaged angular velocity (top) and rotation period (bottom) of a single prolate ellipsoid rotating in Giesekus fluids for different blockage ratios.

respect to x_3-axis. The aspect ratio is $AR = a/b = 2$. The blockage ratio is $K = 2a/H = 0.1$. In order to valid the averaged angular velocity reported in [22], we consider a prolate ellipsoid with its major axis tumbling in x_1x_3-plane (the shear plane). The averaged rotating velocities of prolate ellipsoid reported in Fig. 4 are consistent with those obtained in [22] up to $De = 1.5$. The effect of blockage ratio on the averaged angular velocity is shown in Fig. 5. The two walls do slow down the rotation velocity for larger blockage ratios. For the rotating period shown in Fig. 5, the higher De number does have longer period, which is consistent with those finding reported in, e.g., [20]. Finally, it is interesting to see that, without shear-thinning effect (i.e., $\alpha = 0$), the average rotation velocity is slower in Oldroyd-B fluids as shown in Fig. 6 for larger De numbers.

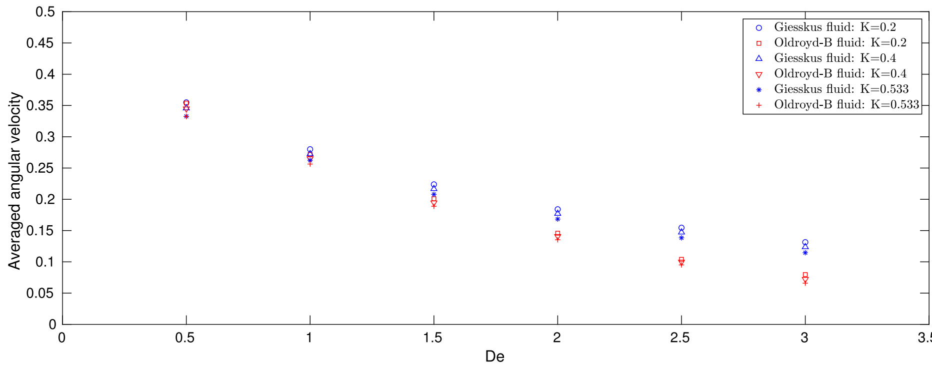

Figure 6: The comparison of averaged angular velocity of a single prolate ellipsoid rotating in Oldroyd-B and Giesekus fluids for different De values.

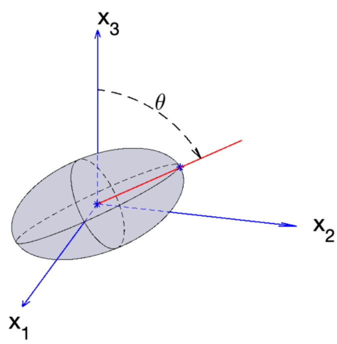

Figure 7: The initial setup of a prolate ellipsoid: Its mass center is fixed at $(0, 0, 0)$. The red line lays on the x_2x_3 plane and the major axis of prolate ellipsoid is the red segment from the center of prolate to the blue "*" on the surface of ellipsoid. The initial angle θ is the angle from x_3 axis to the red line.

3.2. The motions of an ellipsoid in a bounded shear flow

As discussed in Introduction, a prolate ellipsoid rotating dynamics in a bounded shear flow of Giesekus fluids has been studied in [22, 23], and [24]. In this section we like to study its rotating behaviors in a bounded shear flow of Oldroyd-B fluids. The particle inertia effect is taking into account in our study. The fluid density ρ_f and ellipsoid density ρ_s are both equal to 1 g cm^{-3} and viscosity μ_f is 1 poise. The computational domain is $\Omega = (-1.5, 1.5) \times (-1, 1) \times (-0.5, 0.5)$. The shear rate $\dot{\gamma}$ is fixed at 1 sec^{-1}

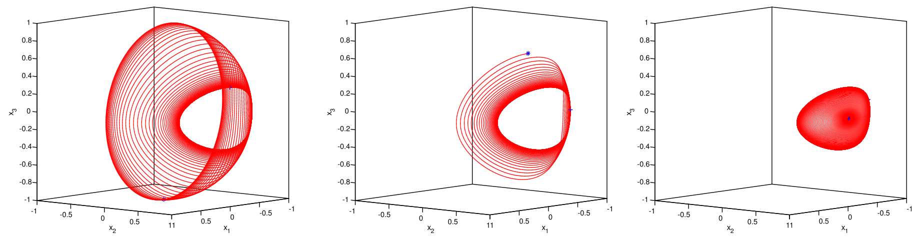

(a) De=0.25

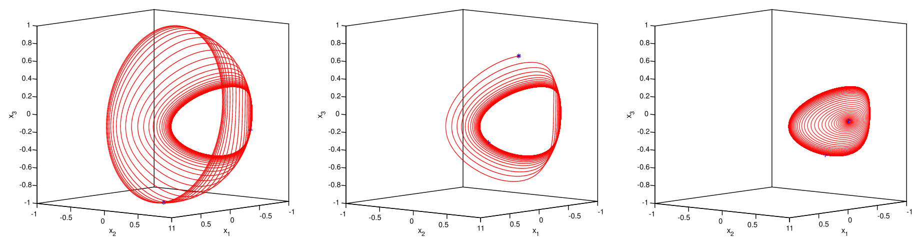

(b) De=0.5

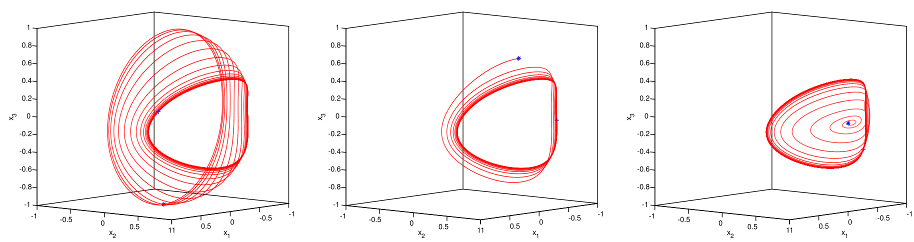

(c) De=1

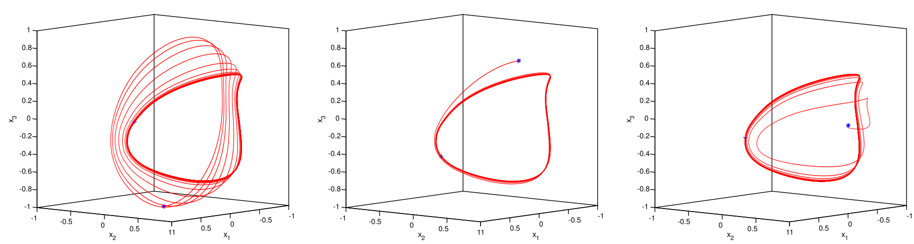

(d) De=2

Figure 8: Kayaking motions: the orientation trajectories of a prolate ellipsoid with three initial angles $\theta = 0°$ (left), $45°$ (middle), and $90°$ (right). The blue "*" (resp., "+") indicates the starting (resp., end) position.

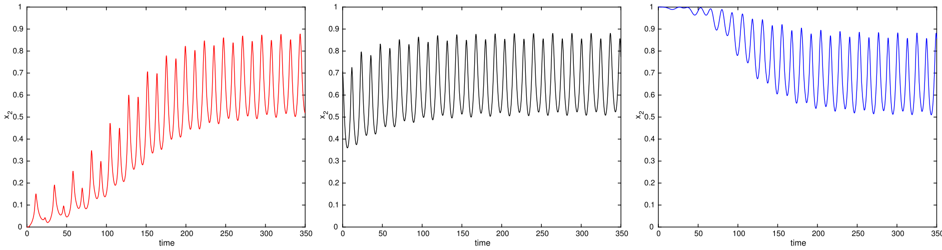

(a) De=1

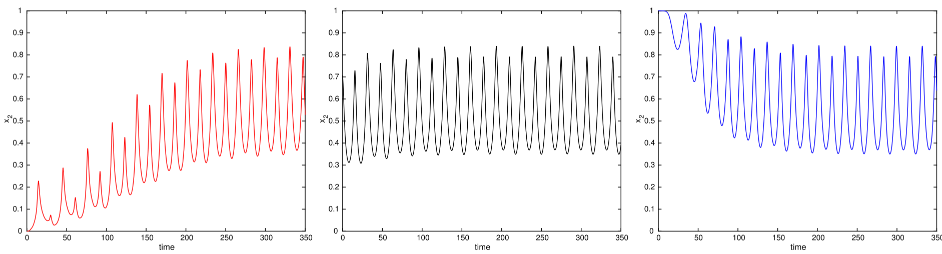

(b) De=1.5

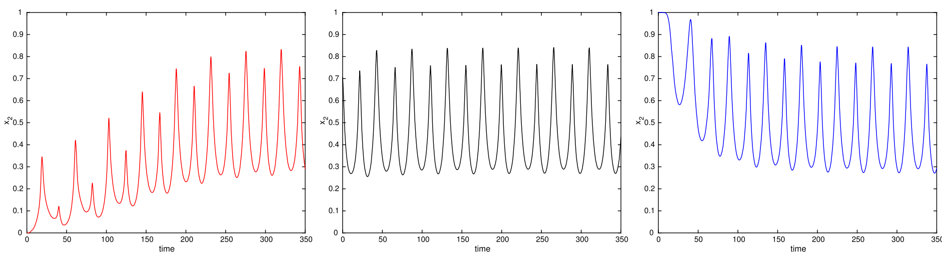

(c) De=2

Figure 9: The x_2-coordinates of the orientation with three initial angles $\theta = 0°$ (left), $45°$ (middle), and $90°$ (right).

so the speed of the top wall is $U = 1$ cm/sec and the speed of bottom wall is $-U = -1$ cm/sec. Then for each Deborah number mentioned later, its relaxation time is $\lambda_1 = De/\dot{\gamma}$ and retardation time is $\lambda_2 = \lambda_1/8$. The semi-major and two semi-minor axes of the ellipsoid are $a = 0.2$, $b = 0.1$, and $c = 0.1$. The aspect ratio is $AR = a/b = 2$. The blockage ratio is $K = 2a/1 = 0.4$. For the initial position of the ellipsoid in Fig. 7, we fix its mass center at (0, 0, 0) and set the major axis and one of the minor axis being on the x_1x_3-

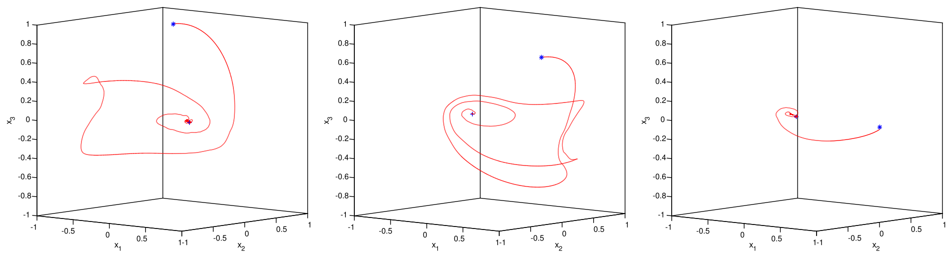

(a) De=3

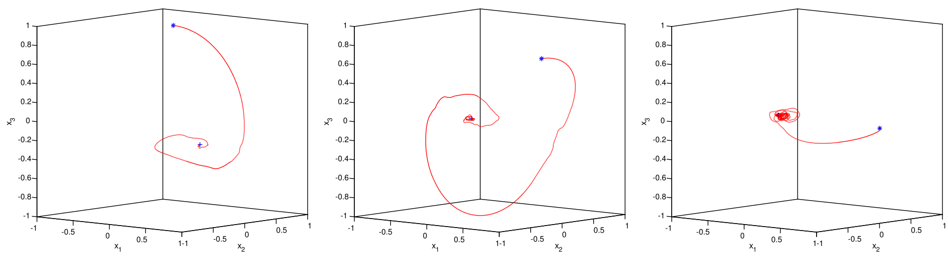

(b) De=4

Figure 10: Log-rolling motion: the orientation trajectories of an ellipsoid with three initial angles $\theta = 0°$ (left), $45°$ (middle), and $90°$ (right). The blue "*" (resp., "+") indicates the starting (resp., end) position.

plane with an initial inclination angle $\theta = 0°, 45°$, and $90°$ with respect to x_3-axis. So the initial tips of the unit vector in the direction of the prolate major axis are (0,0,1) for $\theta = 0°$, $(0, \sqrt{2}/2, \sqrt{2}/2)$ for $\theta = 45°$, and (0,1,0) for $\theta = 90°$, respectively. Since the mass center of prolate ellipsoid is fixed at $(0, 0, 0)$, the prolate orientation can be represented by either the tip of unit vector in the direction of prolate major axis or the tip of a unit vector in the opposite direction. In order to compare the orientations of prolate ellipsoid under different initial angles and Deborah numbers, all the figures are plotted from the points with positive x_2-coordinates.

The orientation trajectories of prolate ellipsoid and histories of x_2-coordinates of the orientation are shown in Figs. 8, 9, 10, and 11 as $De = 0.25, 0.5, 1, 2, 3,$ and 4. For $0.25 \leq De \leq 2$ and $\theta = 0°$, the ellipsoid rotates with the major axis tumbling in the shear plane ($x_2 = 0$) at the beginning. Then the prolate major axis kayaks with respect to the origin and the tip of unit vector leaves the shear plane. Finally, a stable orbit is reached. In Fig. 8, the four left plots are the kayaking motion of prolate ellipsoid with the initial

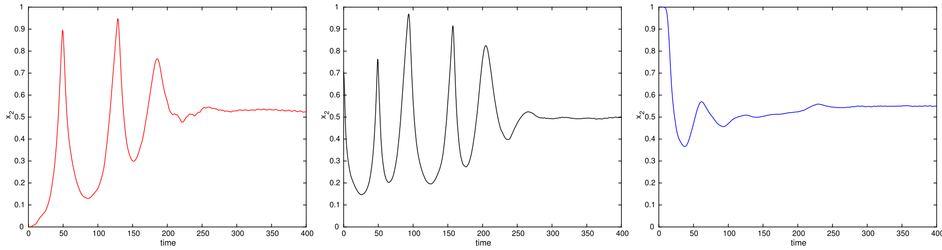

Figure 11: The x_2-coordinates of the orientation with three initial angles $\theta = 0°$ (left), $45°$ (middle), and $90°$ (right) for $De = 3$.

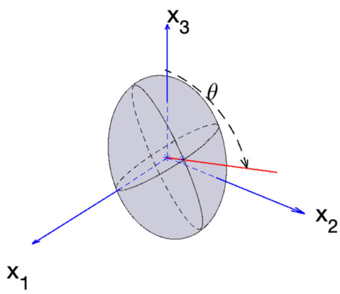

Figure 12: The initial setup of an oblate ellipsoid: Its mass center is fixed at $(0, 0, 0)$. The red line lays on the x_2x_3 plane and the minor axis of oblate ellipsoid is the red segment from the center of prolate to the blue "*" on the surface of ellipsoid. The initial angle θ is the angle from x_3 axis to the red line.

angle of $\theta = 0°$ for $De = 0.25, 0.5, 1$, and 2. Also the three left plots of Fig. 9 show that the x_2-coordinate of orientation unit vector associated with the major axis approaches to a periodic steady state. Similarly, for $\theta = 45°$ and $90°$, the prolate ellipsoid kayaks and its x_2-coordinate of orientation goes to a periodic steady state. For the fluids with same Deborah number, these periodic steady states are basically the same for those three different initial angles. In Fig. 9 (a), the x_2-coordinates of the orientation unit vector go to the periodic steady state after $t = 250$ sec as $De = 1$. We observe the same phenomena as $De = 1.5$ and 2 in Fig. 9 (b) and (c). We also observe a different stable motion as $De = 3$ and 4. Instead of kayaking motion, the major axis of prolate ellipsoid first rotate several times then the tip of unit vector (associated with the major axis) turns forward and the major axis lays down, follows the flow forward direction with certain angle, and at the

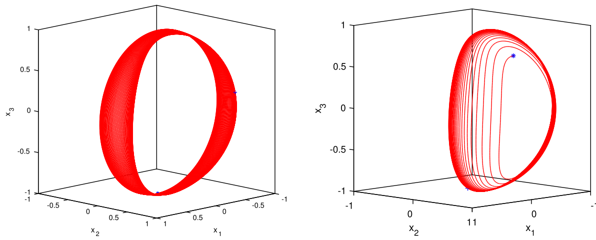

(a) De=0.5

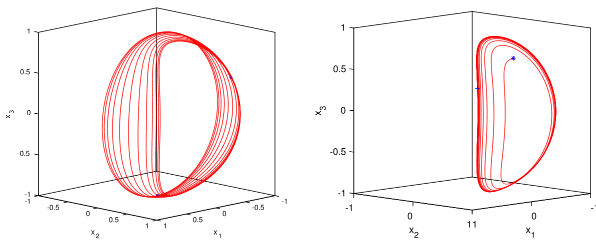

(b) De=1

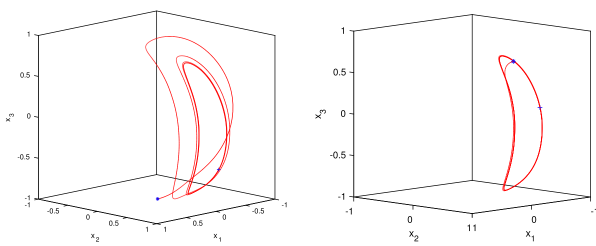

(c) De=2

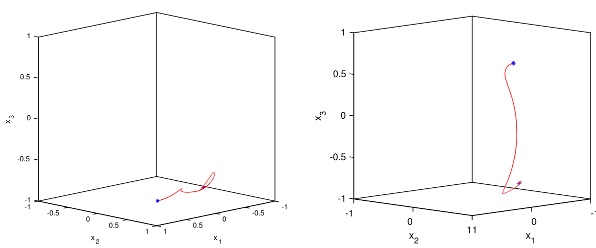

(d) De=2.5

Figure 13: Kayaking motions: the orientation trajectories of an oblate ellipsoid with initial angles $\theta = 0°$ (left) and $45°$ (right) for $De = 0.5, 1,$ and 2. Tilted log-rolling motion: fixed orientation unit vector for $De = 2.5$. The blue "*" (resp., "+") indicates the starting (resp., end) position.

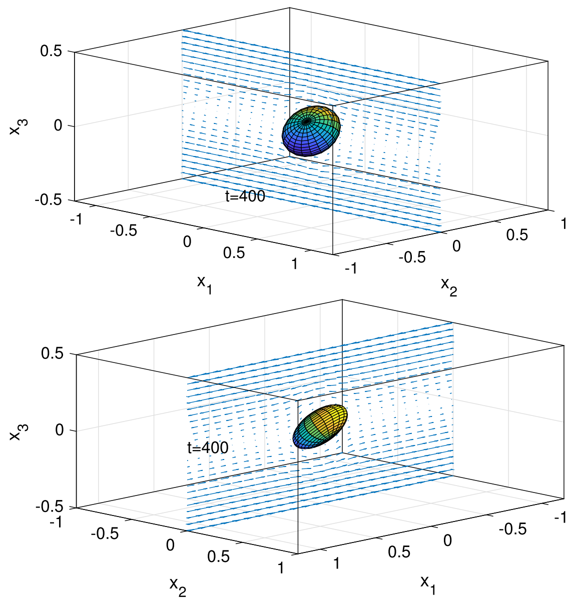

Figure 14: Two different views of the oblate orientation and velocity field projected on the x_1x_3-plane for $De = 2.5$ at $t = 400$.

same time ellipsoid is log-rolling with respect to its major axis as shown in Fig. 10. In Fig. 11, the x_2-coordinates of orientation go from the initial position to the fixed point after $t = 300$. Our results of a prolate rotating in Oldroyd-B fluids are slightly different from the rotating dynamics of a prolate ellipsoid in Giesekus fluids reported in [22, 23], and [24]; but there are some similarities, too. For $De \leq 2$, log-rolling motion is not stable in Oldroyd-B fluids which is similar to the results obtained by Wang *et al.* in [23], but log-rolling is stable in Giesekus fluids when the effect of fluid and particle inertia on the rotation motion was not included as in [22]. For $De = 3$ and 4, the prolate major axis has about a stable fixed direction (up to each initial angle), which is close to those obtained in [22, 23], and [24] for higher De numbers. But like the bistability one obtained in [22], the prolate major axis can reach two different directions as shown in Fig. 10.

To study the rotation behavior of an oblate ellipsoid, we have replaced the prolate considered and discussed previously by an oblate and kept everything else the same. The semi-minor and two semi-major axes of oblate ellipsoid are $a = 0.1$, $b = 0.2$, and $c = 0.2$. Then the aspect ratio is $AR = a/b = 1/2$. With respect to its fixed mass center at (0, 0, 0), the initial inclination angle is either $\theta = 0°$ and $45°$ as explained in Fig. 12. The

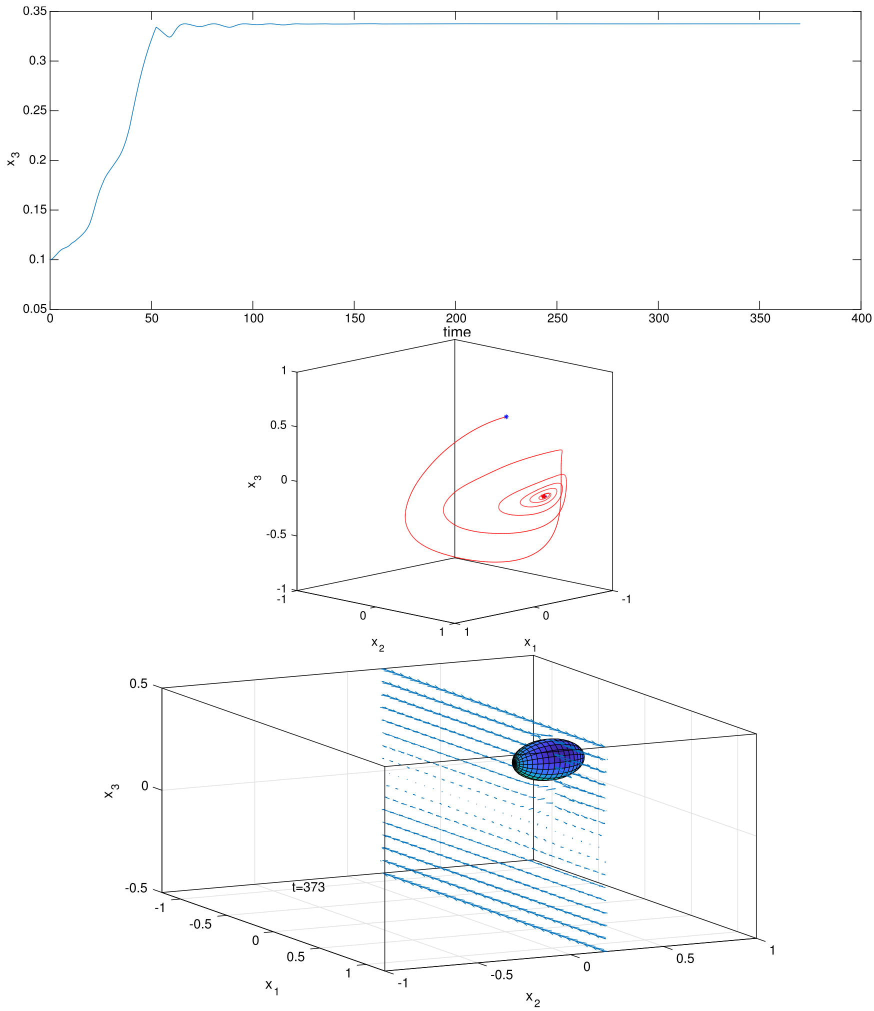

Figure 15: (i) The history of the prolate mass center height (top). (ii) The prolate orientation trajectory with initial angle $\theta = 45°$ (bottom left). (iii) The prolate orientation and velocity field projected on the x_1x_3-plane at $t = 373$ (bottom right).

orientation unit vector for an oblate ellipsoid is the minor axis direction. The minor axis of oblate ellipsoid kayaks as those tip trajectories shown in Fig. 13, which indicates kayaking motion is stable for an oblate rotating in Oldroyd-B fluids for $De = 0.5$, 1, and 2. But for $De = 2.5$, the unit orientation vector turns to a fixed direction and the oblate rotates with respect to it, i.e., the oblate ellipsoid has a stable tilted log-rolling motion (see Figs. 13 and 14). Those results are different from the rotating dynamics of an oblate in a Newtonian fluid obtained in [19].

For a prolate ellipsoid freely moving in a Giesekus fluid, Wang *et al.* [23] obtained that such prolate ellipsoid migrates toward the closer moving wall due to fluid elasticity, and its semi-major axis is slightly away from the vorticity axis direction for $De = 3$. Our prolate ellipsoid considered above is now allowed to move freely in an Oldroyd-B fluid for $De = 3$. We have placed its initial mass center at $(0, 0, 0.1)$ initially with the initial angle $\theta = 45°$. Then later it does migrate next to the top moving wall and its semi-major axis is slightly away from the vorticity axis direction (see Fig. 15) so that the prolate ellipsoid is rolling against the wall. Our result is consistent with the results obtained in [23]. For the oblate considered above with its initial mass center at $(0, 0, 0.1)$ initially with the initial angle $\theta = 45°$, it migrates next to the top moving wall. But its orientation unit vector kayaks (see Fig. 16) in a slightly different way. Thus its mass center is closest to the wall when the orientation unit vector is about parallel to the x_3-direction (i.e., two major axes are about parallel to the x_1x_2-plane); but it is farthest away when the orientation unit vector is about parallel to the x_1x_2-plane (i.e., the oblate lands on edge against the wall).

4. Conclusions

In this article, we have discussed a DLM/FD method for simulating fluid-particle interaction in three-dimensional shear flow of Oldroyd-B and Giesekus fluids. The methodology is validated by comparing the numerical results associated with a neutrally buoyant rigid ellipsoidal particle in Giesekus fluids. For the cases of a prolate ellipsoid placed in the middle between two walls in Oldroyd-B fluids, the simulation results do not depend on initial angles but Weissenberg numbers. As $\mathrm{Wi} = 1, 1.5$, and 2, the prolate ellipsoid kayaks and the x_2-coordinate of its tip is oscillating to a steady state. As $De = 3$, and 4, the ellipsoid first kayaks then its tip turns forward, its major axis follows the flow forward direction with certain angle, and its motion becomes a tilted log-rolling. But like the bistability one obtained in [22], the prolate major axis can reach two different directions.

For an oblate rotating in Oldroyd-B fluids for $De = 0.5$, 1, and 2, kayaking motion is stable. But for $De = 2.5$, the unit orientation vector turns to a fixed direction and the oblate rotates with respect to it, i.e., the oblate ellipsoid has a stable tilted log-rolling motion.

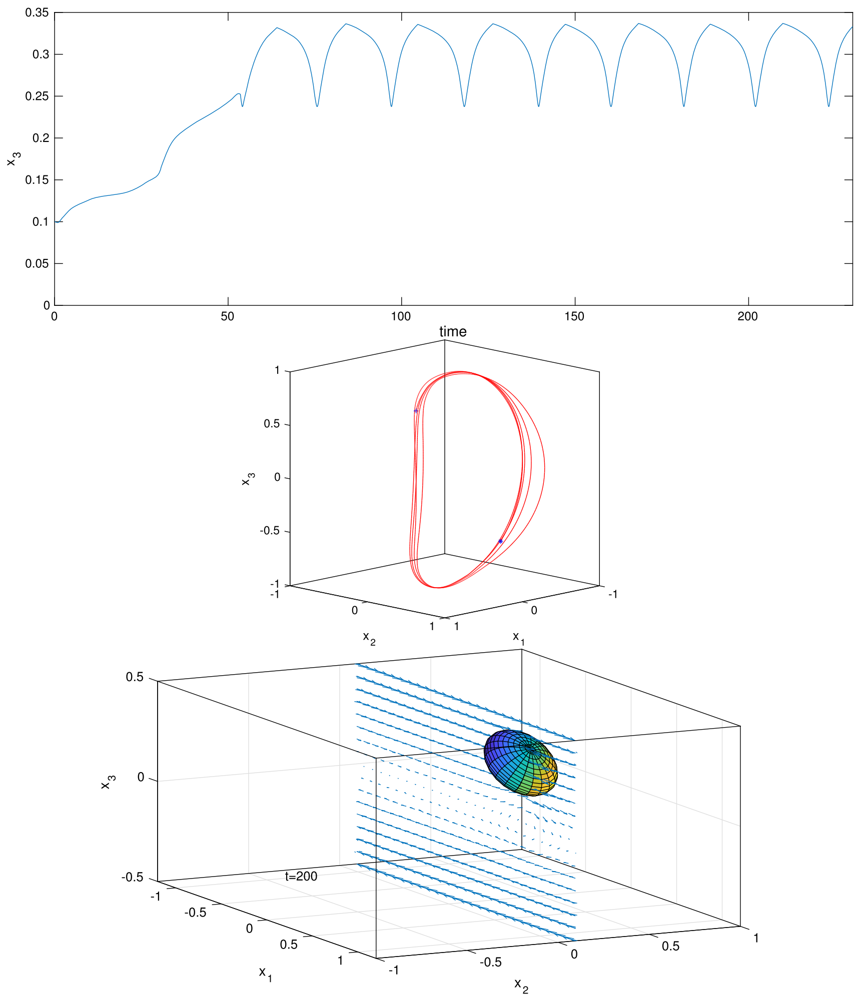

Figure 16: (i) The history of the oblate mass center height (top). (ii) The oblate orientation trajectory with initial angle $\theta = 45°$ (bottom left). (iii) The oblate orientation and velocity field projected on the x_1x_3-plane at $t = 200$ (bottom right).

For a prolate ellipsoid freely moving in an Oldroyd-B fluid, it migrates toward the closer moving wall due to fluid elasticity. It rolls against the wall with its semi-major axis slightly away from the vorticity axis direction for $De = 3$. But for an oblate ellipsoid, it migrates next to the top moving wall and then rolls on the top wall in a way that it lands on edge against the wall periodically.

Acknowledgments

We acknowledge the helpful comments and suggestions of Howard H. Hu (University of Pennsylvania) and James J. Feng (University of British Columbia). Professor Glowinski really liked to develop computational methods for simulating a long-body interacting with Oldroyd-B fluids via direct numerical simulation. He and the two authors, Pan and Chiu, finally did it. But sadly this article was not ready till now.

References

[1] E. A. Molaei, A. B. Yu, and Z. Y. Zhou, Particle scale modelling of solid flow characteristics in liquid fluidizations of ellipsoidal particles. *Powder Tech.* **338** (2018), 677–691.

[2] S. M. J. Sobhani, S. Bazargan, and K. Sadeghy, Sedimentation of an elliptic rigid particle in a yield-stress fluid: A lattice-Boltzmann simulation. *Phys. Fluids* **31(8)** (2019), 081902.

[3] R. Jain, S. Tschisgale, and J. Fröhlich, Impact of shape: DNS of sediment transport with non-spherical particles. *J. Fluid Mech.* **916** (2021), A38. MR4247599

[4] Y. L. Lin, N. J. Derr, and C. H. Rycroft, Eulerian simulation of complex suspensions and biolocomotion in three dimensions. *Proc. Natl. Acad. Sci. U.S.A.* **119(1)** (2021), e2105338118. MR4401222

[5] J. Fu, K. Jiang, S. Chen, and X. Du, Effect of large temperature difference on drag coefficient and Nusselt number of an ellipsoidal particle in compressible viscous flow. *Powder Tech.* **408** (2022), 117766.

[6] G. D'Avino, Numerical simulations on the settling dynamics of an ellipsoidal particle in a viscoelastic fluid. *J. Non-Newtonian Fluid Mech.* **310** (2022), 104947. MR4514795

[7] Y. Zhao, P. Zhang, L. Lei, L. Kong, S. A. Galindo-Torres, and S. Z. Li, Metaball-Imaging discrete element lattice Boltzmann method for fluid–particle system of complex morphologies with case studies. *Phys. Fluids* **35(2)** (2023), 023308.

[8] A. R. Gollakota, and N. Kishore, CFD study on rise and deformation characteristics of buoyancy-driven spheroid bubbles in stagnant Carreau model non-Newtonian fluids. *Theor. Comput. Fluid Dyn.* **32** (2018), 35–46. MR3928695

[9] T. Zhang, Y. Qian, J. Yin, B. Zhang, and D. Wang, Experimental study on 3D bubble shape evolution in swirl flow. *Exp. Therm. Fluid Sci.* **102** (2019), 368–375.

[10] B. Ji, Q. Song, and Q. Yao, Impact of hydrophobic micron ellipsoids on liquid surfaces. *J. Colloid Interface Sci.* **532** (2018), 711–717.

[11] N. Ballard, A. D. Law, and S. A. Bon, Colloidal particles at fluid interfaces: behaviour of isolated particles. *Soft Matter* **15(6)** (2019), 1186–1199.

[12] A. M. Luo, J. Vermant, P. Ilg, Z. Zhang, and L. M. Sagis, Self-assembly of ellipsoidal particles at fluid-fluid interfaces with an empirical pair potential. *J. Colloid Interface Sci.* **534** (2019), 205–214.

[13] S. Trevenen, and P. J. Beltramo, Gradient stretching to produce variable aspect ratio colloidal ellipsoids. *J. Colloid Interface Sci.* **583** (2021), 385–393.

[14] J. A. Arguedas-Leiva, and M. Wilczek, Microswimmers in an axisymmetric vortex flow. *New J. Phys.* **22(5)** (2020), 053051. MR4127602

[15] H. Amini, W. Lee, and D. Di Carlo, Inertial microfluidic physics. *Lab on a Chip* **14(15)** (2014), 2739–2761.

[16] G. D'Avino, and P. L. Maffettone, Particle dynamics in viscoelastic liquids. *J. Non-Newtonian Fluid Mech.* **215** (2015), 80–104. MR3401241

[17] Z. Li, and J. Lin, On the some issues of particle motion in the flow of viscoelastic fluids. *Acta Mechanica Sinica* **38(3)** (2022), 321467.

[18] G. B. Jeffery The motion of ellipsoidal particles immersed in a viscous fluid. *Proc. R. Soc. Lond. A* **102** (1922), 161–79.

[19] J. Einarsson, F. Candelier, F. Lundell, J. R. Angilella, and B. Mehlig, Effect of weak fluid inertia upon Jeffery orbits. *Phys. Rev. E* **91** (2015), 041002. MR3476365

[20] D. Z. Gunes, R. Scirocco, J. Mewis, and J. Vermant, Flow-induced orientation of non-spherical particles: effect of aspect ratio and medium rheology. *J. Non-Newtonian Fluid Mech.* **155** (2008), 39–50.

[21] S. A. Abtahi, and G. J. Elfring, Jeffery orbits in shear-thinning fluids. *Phys. Fluids* **31** (2019), 103106.

[22] G. D'Avino, M. A. Hulsen, F. Greco, P. L. Maffettone, Bistability and metabistability scenario in the dynamics of an ellipsoidal particle in a sheared viscoelastic fluid. *Phys. Rev. E* **89** (2014), 043006.

[23] Y. Wang, Z. Yu, and J. Lin, Numerical simulations of the motion of ellipsoids in planar Couette flow of Giesekus viscoelastic fluids. *Microfluidics and Nanofluidics* **23** (2019), 1–16.

[24] Y. Li, C. Xu, and L. Zhao, Rotational dynamics of a neutrally buoyant prolate spheroid in viscoelastic shear flows at finite Reynolds numbers. *J. of Fluid Mech.* **958** (2023), A20. MR4555326

[25] T.-W. Pan, A. Guo, S.-H. Chiu, and R. Glowinski, A 3D DLM/FD method for simulating the motion of spheres and ellipsoids under creeping flow conditions. *J. Comput. Phys.* **352** (2018), 410–425. MR3717144

[26] S.-H. Chiu, T.-W. Pan, and R. Glowinski, A 3D DLM/FD method for simulating the motion of spheres in a bounded shear flow of Oldroyd-B fluids. *Computers & Fluids* **172** (2018), 661–673. MR3832061

[27] J. Hao, T.-W. Pan, R. Glowinski, and D. D. Joseph, A fictitious domain/distributed Lagrange multiplier method for the particulate flow of Oldroyd-B fluids: A positive definiteness preserving approach. *J. Non-Newtonian Fluid Mech.* **156** (2009), 95–111.

[28] A. Lozinski, and R. G. Owens, An energy estimate for the Oldroyd-B model: theory and applications. *J. Non-Newtonian Fluid Mech.* **112** (2003), 161–176.

[29] R. Glowinski, T.-W. Pan, T. I. Hesla, and D. D. Joseph, A distributed Lagrange multiplier/fictitious domain method for particulate flows. *Int. J. Multiphase Flow* **25** (1999), 755–794. MR2436653

[30] P. Singh, D. D. Joseph, T. I.Hesla, R. Glowinski, and T.-W. Pan, A distributed Lagrange multiplier/fictitious domain method for viscoelastic particulate flows. *J. Non-Newtonian Fluid Mech.* **91** (2000), 165–188. MR2436653

[31] R. Glowinski, T.-W. Pan, T. I. Hesla, D. D. Joseph, and J. Périaux, A fictitious domain approach to the direct numerical simulation of incompressible viscous flow past moving rigid bodies: Application to particulate flow. *J. Comput. Phys.* **169** (2001), 363–426. MR1836521

[32] T.-W. Pan and R. Glowinski, Direct simulation of the motion of neutrally buoyant circular cylinders in plane Poiseuille flow. *J. Comput. Phys.* **181** (2002), 260–279. MR1925983

[33] T.-W. Pan and R. Glowinski, Direct simulation of the motion of neutrally buoyant balls in a three-dimensional Poiseuille flow. *C. R. Mecanique, Acad. Sci. Paris* **333** (2005), 884–895.

[34] T.-W. Pan, C.-C. Chang, and R. Glowinski, On the motion of a neutrally buoyant ellipsoid in a three-dimensional Poiseuille flow. *Comput. Methods Appl. Mech. Engrg.* **197** (2008), 2198–2209. MR2412820

[35] T.-W. Pan and S.-H. Chiu, A DLM/FD method for simulating balls settling in Oldroyd-B viscoelastic fluids. *J. Comp. Phys.* **484** (2023), 112071. MR4569233

[36] D. D. Joseph, *Fluid Dynamics of Viscoelastic Liquids*. Springer (1990). MR1051193

[37] G.-J. Li, A. Karimi, A. M. Ardekani, Effect of solid boundaries on swimming dynamics of microorganisms in a viscoelastic fluid. *Rheol. Acta* **53** (2014), 911–926.

[38] G. Schleiniger, R. J. Weinacht, A remark on the Giesekus viscoelastic fluid. *J. Rheol.* **35** (1991), 1157–1170.

[39] M. O. Bristeau, R. Glowinski, and J. Périaux, Numerical methods for the Navier-Stokes equations. Applications to the simulation of compressible and incompressible viscous flow. *Comput. Phys. Reports* **6** (1987), 73–187. MR0913308

[40] R. Glowinski, Finite element methods for incompressible viscous flows. In: *Handbook of Numerical Analysis, vol. IX*, pp. 3–1176. North-Holland, Amsterdam (2003). MR2009826

[41] C. S. Peskin, Numerical analysis of blood flow in the heart. *J. Comput. Phys.* **25** (1977), 220–252. MR0490027

[42] C. S. Peskin, and D. M. McQueen, Modeling prosthetic heart valves for numerical analysis of blood flow in the heart. *J. Comput. Phys.* **37** (1980), 113–32. MR0584324

[43] C. S. Peskin, The immersed boundary method. *Acta Numer* **11** (2002), 479–517. MR2009378

[44] J. Chorin, T. J. R. Hughes, M. F. McCracken, and J. E. Marsden, Product formulas and numerical algorithms. *Commun. Pure Appl. Math.* **31** (1978), 205–256. MR0488713

[45] R. Glowinski and T.-W. Pan, *Numerical Simulation of Incompressible Viscous Flow: Methods and Applications*, De Gruyter, Berlin/Boston (2022). MR4687183

[46] T.-W. Pan, S. Zhao, N. Niu, and R. Glowinski, A DLM/FD/IB method

for simulating compound vesicle motion under creeping flow condition. *J. Comput. Phys.* **300** (2015), 241–253. MR3396257

[47] T.-W. Pan, R. Glowinski, On the dynamics of particle sedimentation in viscoelastic fluids: A numerical study on particle chaining in two-dimensional narrow channels. *J. Non-Newtonian Fluid Mech.* **244** (2017), 44–56. MR3652860

[48] E. J. Dean, and R. Glowinski, A wave equation approach to the numerical solution of the Navier-Stokes equations for incompressible viscous flow. *C.R. Acad. Sci. Paris Ser. 1* **325** (1997), 783–791. MR1483718

[49] J. R. Whiteman, and G. Goodsell, A survey of gradient superconvergence for finite element approximation to second order elliptic problems on triangular tetrahedral meshes. In: Whiteman J. R. editor, *The Mathematics of Finite Elements and Applications VII*, pp. 55–74. Academic Press, London (1991). MR1132486

Shang-Huan Chiu
Department of Mathematics
Lehigh University
Bethlehem, PA 18015
USA
E-mail address: schiu.twn@gmail.com
URL: http://math.cas.lehigh.edu/shang-huan-chiu-0

Tsorng-Whay Pan
Department of Mathematics
University of Houston
Houston, TX 77204
USA
E-mail address: pan@math.uh.edu
URL: https://www.math.uh.edu/~pan

Received June 1, 2023